Electron energy relaxation in disordered superconducting NbN films

Mariia Sidorova, Alexej Semenov, and Heinz-Wilhelm Hübers
Institute of Optical Sensor Systems, German Aerospace Center (DLR), Rutherfordstrasse 2, 12489 Berlin, Germany

Konstantin Ilin, and Michael Siegel,
Institut für Mikro- und Nanoelektronische Systeme (IMS), Karlsruher Institut für Technologie (KIT), Hertzstr. 16, 76187 Karlsruhe, Germany

Ilya Charaev
Department of Electrical Engineering and Computer Science, Massachusetts Institute of Technology, Cambridge, Massachusetts 02139, USA

Maria Moshkova
National Research University Higher School of Economics, Moscow, Russia, Department of Physics, Moscow Pedagogical State University, 29 Malaya Pirogovskaya St, Moscow, 119435,Russia, and 2 LLC "Superconducting Nanotechnology" (SCONTEL), Moscow, 119021, Russia

Natalia Kaurova
Department of Physics, Moscow Pedagogical State University, 29 Malaya Pirogovskaya St, Moscow, 119435, Russia

Gregory N. Goltsman
Department of Physics, Moscow Pedagogical State University, 29 Malaya Pirogovskaya St, Moscow, 119435,Russia and National Research University Higher School of Economics, Moscow, Russia

Xiaofu Zhang and Andreas Schilling
Physics Institute, University of Zürich, Winterthurerstrasse 190, 8057 Zürich, Switzerland

ABSTRACT

We report on the energy relaxation of electrons studied by means of magnetoconductance and photoresponse in a series of superconducting NbN film with thickness in the range from 3 to 33 nm. The inelastic scattering rate of electrons on phonons obeys T^n temperature dependence where the exponent is in the range $n \approx 3.2 \div 3.8$ and shows no systematically dependence on the degree of disorder. At 11 K electron-phonon scattering times are in the range 11.9 - 17.5 ps. We show that in the studied NbN films the Debye temperature and the density of phonon states are both reduced with respect to bulk material. In the thinnest studied films reduced density of states along with the phonon trapping slows down the energy relaxation of electrons by a factor of 4 as compared to the prediction of the tree dimensional phonon model.

I. INTRODUCTION

Energy relaxation of nonequilibrium electrons plays an essential role in physics of superconducting detectors. The most important relaxation processes are inelastic electron-phonon scattering and phonon escaping since they determine directly timing metrics in the performance of practical detectors. Advanced theoretical models e.g. those of superconducting nanowire single-photon detector (SNSPD) [1] or hot-electron bolometers (HEB) [2, 3] involve not only electron-phonon scattering time, $\tau_{e\text{-}ph}$, and phonon escape time, τ_{esc} but also a few other key parameters. These are the ratio between electron and phonon heat capacities, c_e/c_{ph}, the density of electronic states at the Fermi level, and the diffusivity of electrons. Together with scattering times they affect the energy transfer from electromagnetic radiation to electrons and further to the surrounding.

Electron-phonon scattering in bulk and clean metals is thoroughly described theoretically [4] as well as the acoustic mismatch model describes escape of isotropic, three dimensional (3-d) Debye phonons from metal to

dielectric through a plane boundary [5]. However, practical devices usually exploit thin and disordered superconducting films. For instance, SNSPD with the record detection efficiency of 94% utilizes NbN film with a normal-state resistivity 5.7×10^3 Ohm nm [6] that is much larger than the resistivity ≈ 550 Ohm nm of crystalline stoichiometric NbN films [7]. The theory of clean metals doesn't describe electron-phonon scattering in such films, since the scattering is modified by disorder and impurities. One of the most advanced theories of electron-phonon scattering in disorder metals has been developed by Sergeev and Mitin (SM) [8]. The SM theory predicts that, depending on the degree of disorder and the kind of impurities, the exponent, *n*, in the power dependence of the electron-phonon scattering rate $1/\tau_{e\text{-}ph} \propto T^n$ can have a value between 2 and 4. Furthermore, the phonon spectrum in an ultrathin film necessarily deviates from the Debye spectrum, which is commonly assumed in theories but is inherent only in bulk crystalline solids. In thin films at low temperatures the mean free path and the wavelength of phonons become comparable or even larger than the film thickness that destroys isotropy of the phonon spectrum and reduces phonon density of states. The reduced density of states affects the strength of electron-phonon scattering and modifies its temperature dependence [9, 10] while reduced isotropy obstructs phonon escaping. Under these conditions the classic acoustic mismatch model [5] doesn't describe anymore phonon escape from the film to the substrate. The degree of phonon anisotropy depends crucially not only on the phonon wavelength relatively to the film thickness but also on the acoustic match between the film and the substrate [9, 11-13]. Attempts to account for phonon anisotropy and reduced density of states were made phenomenologically in Refs. 14 and 13 and microscopically in Ref. 12. The authors of Ref. 13 divided phonons into two groups and assigned them different heat capacities and different abilities to leave the film. The approach is referred as the three-temperature model. Its results agree with the prediction of the microscopic model [12]. Another approach is called ray tracing [14]. The authors of Ref. 14 took into account breaking of Cooper pairs by phonons along with phonon scattering at non-paired electrons and traced phonons over several scattering events and reflections from the film surfaces. They showed that phonon trapping slows down the energy transfer from electrons to the substrate and that for sufficiently thin films the rate of the energy transfer does not decrease anymore with the further decrease in the film thickness.

Additionally to complications described above, material parameters of films, which are used for producing practical devices, can be hardly predicted theoretically. Knowledge of these parameters has to be acquired experimentally. For example, niobium nitride, that is a conventional material for SNSPD, has been widely studied by means of various experimental techniques. However, significant discrepancies are present between data that have appeared in literature over the past three decades. Actually, it is not entirely surprising. Over the years the fabrication process of NbN films has been optimized that definitely resulted in variations of material parameters.

Undoubtedly, it is necessary to revise the problem of energy relaxation in thin superconducting NbN film. To achieve this goal, we first analyzed relaxation rates in NbN films reported in literature (subsection A below) as well as the experimental techniques and models which the authors used to describe their data (subsection B). Second, we measured by means of different experimental techniques relaxation rates and relevant parameters in two series of NbN films which were deposited with different regimes on different substrates. In Section II we describe these regimes and parameters of specimens used for our study. Sec. III A-B provides a description of transport and magnetoconductance measurements from which we extract values of electron-phonon scattering time and its temperature dependences. Sec. III C contains data obtained with the time-domain technique from which we estimate a ratio between electron and phonon heat capacities. Scattering rates obtained from the photoresponse in the frequency domain are described in Section II D. We analyze our data in Section IV. Section IV A contains a comparison between our experimental data and predictions of the SM model. Fitting experimental data with the model allows us to extract acoustic parameters of our films. With these parameters we evaluate (Sec. IV B) transmission coefficients for phonons at the film interfaces and estimate escape time for phonons in the framework of the acoustic mismatch model. In Sec. IV C we apply phonon ray-tracing to account for phonon trapping and to describe our experimental data on the electron-energy relaxation time as a function of the film thickness. We summarize our results in Section V.

A. Reported relaxation rates in NbN films

In Table I we summarize published electron-phonon scattering times, phonon escape times and heat capacity ratios for NbN films of various thicknesses on different dielectric substrates that have been measured by means of different experimental techniques. We also include publications reporting on transport parameters obtained via Hall and magnetoconductance measurements.

Table I. Reported characteristics of NbN films: T_C transition temperature, d film thickness, R_{SN} resistance of the film square at $T > T_C$. Transport parameters of electrons in the normal state are diffusivity, D, elastic mean free path, l, and elastic scattering time, τ. AMAR – Absorption of Modulated (Amplitude) sub-THz Radiation [15], 2-T – two-temperature model for electrons and phonons [16], MC – magnetoconductance.

d, nm	T_C, K	$R_{SN,}$ Ohm	$\tau_{e\text{-}ph}(T)$, ps	n	$c_e/c_{ph}(T)$	τ_{esc}, ps	Substrate	D, cm^2/s	l, nm	τ, fs	Experimental technique & analysis	Ref.
15 – 30	11.0 – 12.0	200 – 60	20(10)[a]	1[a]			Al_2O_3				AMAR & 2-T	[17]
5	8.5	450				115	Si/Si_3N_4				Time domain & 2-T	[18]
200 - 300	10.3	34 – 20	7.2(10)	1.64			Si/SiO_2	0.2			MC	[19]
2.5 -10		1000 – 70				32.5 - 130	Al_2O_3				AMAR & 2-T	[20]
20	8.2	360	17(8)		0.3(8)	160	MgO				Time-domain & 2-T	[21]
7	11.0	500	12(7)[a]	1.6[a]			Al_2O_3	0.4	0.1		AMAR & 2-T	[22]
3.5	10.6	400-500	10(10)			38	Al_2O_3				Time-domain & 2-T	[23]
3.2 - 14.4	9.9 – 15.3	831 – 81					Al_2O_3	0.51 – 0.66	0.58 – 0.83	2.16 – 3.86	Ellipsometry	[24]
12	14.96	85					Al_2O_3	0.83	0.2		Hall measurements	[25]
2.16 – 15	6.7 – 15.0	2377 – 107					Al_2O_3				Tunneling spectroscopy	[26]
>50	9.99 – 16.11	189.2 -76.6					MgO		0.207 – 0.396		Hall & transport measurements	[27]
6	12.63	431						0.544				[28]
2 -20.5	2.6 – 15.0	1200 – 40					MgO	1.04 – 0.76	0.13 – 0.27	0.1	MC	[29]
5.2	11.15	257.7		3			MgO	0.9			MC	[30], [31]
5.5 7	13.51 7.71	280 803					MgO Si/SiO_2	0.92 0.47			Hall & transport measurements	[32]
5.5	7.84	640			0.7(8)		Si/SiO_2	0.35			Resistive thermometry & 2-T	[33]

[a] The authors identified measured decay times of the photoresponse with the electron-phonon relaxation time $\tau_{e\text{-}ph}$. The exponent n relates to the temperature dependence of the photoresponse time.

For all films in Table I, the resistivity, $R_{SN}\,d$ (R_{SN} is the resistance of the film square, d is the film thickness), is much larger than the resistivity ≈ 550 Ohm nm of crystalline stoichiometric NbN films [7]. Although magnitudes of $\tau_{e\text{-}ph}$ are close for a few different films in Table I, the exponent n in the power dependence of $\tau_{e\text{-}ph}^{-1}$ on temperature varies from 1 to 3. Since for reported films the magnitudes of inelastic (electron-phonon) scattering time, $\tau_{e\text{-}ph} >> \tau$, where τ is the elastic scattering time of electrons, they are supposed to exhibit the phenomenon of weak electron localization.

The elastic mean free path, l, is of the order of the interatomic distance in stoichiometric NbN (0.44 nm) and the electron diffusivity in the normal state stays in the range $0.2 \le D \le 1$ cm^2/s. Quantities related to the metal-insulator transition (Ioffe-Regel parameter $k_F l$) and the degree of disorder fall in the intervals $1.5 \le k_F l \le 7.1$ and $0.015 \le q_T l \le 0.54$, respectively, where q_T is the wave vector of thermal phonons and k_F is the wave vector of electrons at the Fermi energy. This classifies the films from Table I as disordered films ($q_T l << 1$) close to the Anderson localization limit $k_F l = 1$.

By means of numerical simulations, it has been shown that the condition $k_F l \approx 1$ converts superconductor into a granular system where superconducting grains (islands) are immersed in an insulating sea and interconnected by Josephson junctions [34]. The granular morphology of thick NbN film was observed in Ref. 35. Unusually small value of the electron diffusion coefficient in thick films reported in Ref. 19 indicates either presence of defects (vacancies or impurities) or pronounced granularity [25] that should definitely affect the inelastic scattering rate of electrons [36].

Regarding phonon escape time, the values shown in Table I noticeably exceed values estimated in the framework of the classical isotropic model [5] as $\tau_{esc} = 4d/(\bar{\eta}\,\bar{u})$, where $\bar{\eta}$ is the mean transmission of the film/substrate interface for phonons, and $\bar{u}$ is the mean sound velocity in the film (Section IV B).

B. Electron energy relaxation: Measuring techniques and models

There are several experimental methods which allow finding the magnitude and the temperature dependence of the relaxation rate of the electron energy. We divide all them into two broad groups of steady-state and dynamic methods according to whether the measured parameter does not vary or does vary in time. The former group includes photoresponse in the frequency domain to amplitude-modulated radiation (FDAM) in the spectral range from sub-THz [15] to optics [37], magnetoconductance (MC) [38] and resistive thermometry [33]. The latter group includes photoresponse in the time domain to a short pulse (TDP) excitation.

It is worth mentioning here assumptions that resistive thermometry, FDAM and TDP techniques imply. The measurements rely on radiation-induced change in the resistance, which deals with either vortices (realm of BKT physics) or normal domain along the current path, but the response is described in terms of quasiparticles and Cooper pairs (realm of non-equilibrium superconductivity). The techniques are applied under similar operating conditions, i.e. the current-carrying microbridge is kept at the superconducting transition and is illuminated by electromagnetic radiation with varying intensity. The intensity of incident electromagnetic radiation is modulated either periodically (FDAM) or by forming pulses (TDP).The measured quantity is the voltage drop over the current path in the microbridge which changes when the resistance of the microbridge changes. The change in resistance is caused by variation in the absorbed power of electromagnetic radiation. Absorbed energy is transferred to electrons and increases their temperature but it doesn't change the resistance. The resistance is determined by the density of free vortices or by the size of the normal domain. It is assumed that the vortex density or the size of the domain instantly follows the electron temperature which quickly adjusts itself to the absorbed energy. Crucial to these techniques is small absorbed power that ensures the linearity of the photoresponse and exponential relaxation.

The MC technique allows finding phase-breaking rate of the electron wave function for conductors in the quantum diffusive regime when electrons undergo multiple elastic (phase preserving) scattering events before the coherence (phase) of the wave function is randomized due to any inelastic (phase breaking) scattering event. In this regime conducting electrons experience quantum interference leading to an enhanced probability for backscattering

(returning to the initial position after several scattering events). This quantum phenomenon is called weak localization (WL) and results in a negative correction to the normal Drude conductivity. The magnitude of this correction increases when the temperature decreases. Magnetic field breaks symmetry of time-reversed loop trajectories and destroys the enhanced backscattering. Since the maximum length of trajectories contributing to WL is limited to the inelastic scattering length, this length can be evaluated by measuring the field that suppresses WL. Corresponding phase-breaking rate is a sum of rates of all inelastic scattering processes. Electron-phonon scattering dominates in phase-breaking at temperatures well above T_C. In the vicinity of T_C, phase-breaking and the correction to the conductivity are additionally affected by superconducting fluctuations (see details in Sec. III B).

Electron-phonon scattering rates, which all aforementioned methods deliver, are averaged over electron ensemble [21] and therefore differ from the single-particle scattering rates. Depending on operating conditions and the kind of excitation non-equilibrium electrons obey different distribution functions that causes different averaged outcomes. Below we discuss qualitatively how distribution function is modified by each experimental technique and how it affects the measured scattering rate.

MC technique operates with very small currents which do not heat electrons. Therefore, they retain equilibrium distribution function. Extracted $\tau_{e\text{-}ph}^{-1}$ is averaged over electrons from a narrow k_BT layer and is close to the single-particle scattering rate at Fermi energy. In AMAR technique one applies excitation in the sub-THz range where quantum energy is close to or slightly larger than k_BT_C. This excitation slightly increases the effective temperature of electrons. The distribution function retains the equilibrium form corresponding to the increased electron temperature. Here again $\tau_{e\text{-}ph}^{-1}$ is averaged over the ensemble of electrons from the narrow energy layer which is slightly larger than the energy layer relevant to the MC technique. As a result, scattering rates obtained by means of AMAR technique should not differ much from those obtained with MC technique. In FDAM and TDP techniques one applies excitation in the visible or near infrared range where photon energy is much larger than k_BT_C. This excitation results in a quasi-equilibrium distribution function with a tail extended to larger energies [39]. The measured time is an average over the entire distribution with the tail. Since single-particle scattering time $\tau_{e\text{-}ph}$ decreases with the increase of the electron energy, FDAM and TDP techniques can provide underestimated $\tau_{e\text{-}ph}$ values.

Data analysis in resistive thermometry, AMAR, FDAM and TDP methods is based on the two-temperature (2-T) model [16] which is an extension of the Rothwarf-Taylor model [40]. The latter describes the dynamics of excited quasiparticles and phonons at temperatures much smaller than T_C when they are characterized by their number densities rather than distribution functions. At temperatures close to T_C, Rothwarf-Taylor model can be linearized and the resulting equations become mathematically equivalent to those of the 2-T model. The 2-T model implies that electrons and phonons are instantly in the internal equilibrium and are described by their equilibrium distribution functions with two different effective temperatures which both are slightly larger than the ambient temperature. The evolution of the effective temperatures caused by external excitation is described by a system of coupled time-dependent equations. It is further assumed that the rate of the decay of the excess phonon energy is a sum of rates τ_{esc}^{-1} and $\tau_{\mathrm{ph-e}}^{-1}$ associated with escaping of phonons from the film into the substrate and with emitting electrons, respectively ($\tau_{ph\text{-}e}$ is the characteristic phonon-electron scattering time). Hence, the model neglects implicitly phonon trapping that occurs when the mean free path of phonons with respect to electron emission becomes larger than the thickness of the film [14]. The principle of detailed balance [40] requires that in the equilibrium the energy flow from electrons to phonons equals the backward flow. This equality relates the heat capacity ratio to the ratio of scattering times for electron and phonons as $c_e/c_{ph} = \tau_{e\text{-}ph}/\tau_{ph\text{-}e}$ [16]. In the framework of the 2-T model it is possible to account for phonon softening [41], reduction of phonon dimensionality and the anisotropy of the phonon spectrum inherent in thin films by assigning to all phonons an effective escape time τ_{esc}^{*} that differs from the value derived from the acoustic mismatch model and relates to the phonon-electron scattering time via the bottleneck parameter $\gamma = \tau_{\mathrm{ph-e}}/\tau_{esc}^{*} = \tau_{\mathrm{e-ph}}/\tau_{\mathrm{esc}}\ (c_{\mathrm{ph}}/c_{\mathrm{e}})$ [42]. Alternatively, one can use the escape time of the acoustic mismatch model and assign to phonons an effective heat capacity; which differ from the Debye value [13].

II. SPECIMENS AND PARAMETERS

We studied thin NbN films with different thickness and different degrees of disorder. The specimens are listed in Table II. Films of the A-series (2559, A853, A854 and A855) were onto silicon substrates on top of a thermally prepared layer of silicon oxide with a thickness of 250 nm. Magnetoconductance measurements (Sec. III B) were carried out with non-structured approximately squared 1x1 cm^2 NbN films. TDP measurements (Sec. III C) were carried out with the same films which were shaped in the form of microbridges. The lengths of microbridges varied from 3.6 to 7 μm and the widths from 0.615 to 0.69 μm. in order to match the normal square resistance of each microbridge to the electrical impedance of the readout circuit. FDAM measurements (Sec. III D) were carried out with a series of NbN microbridges on sapphire substrates (K1 - K9). They had thicknesses in the range from 3.2 to 33.2 nm. Films of these series were also magnetron-sputtered. The sputtering regime was optimized for the largest T_C. The fabrication process of these K-films is described in detail in Refs. 37 and 43. Below in Section III A we describe how the total density of electronic states, transition temperature and diffusivity were estimated.

As seen from the Table II, the films of similar thicknesses 2259, A853 and K2 are characterized by different degree of disorder. Indeed, diffusion coefficient, transition temperature and the density of states, $N(0)$, of the film K2 is larger as compared to films 2259 and A853, while the square resistance, R_{SN}, is lower. The numbers indicate that the composition of the film K2 is characterized by $x < 0$ (stoichiometric composition Nb_xN_{1-x}, x=0) and a higher content of niobium than the composition of films 2259 and A853 [Ref. 43, Chapter 3]. Among all films, the film A853 has the largest degree of disorder and is close to the superconductor-insulator transition [34].

Table II. Parameters of studied NbN films. R^{300K}/R^{20K} is the ratio of the resistances at 300 and 20 K, $N(0)$ is the total density of states for electrons at Fermi energy.

Sample	d (nm)	T_C (K)	R_{SN} (20K) (Ohm/sq)	D (10^{-4} m^2/s)	$N(0)$ (eV^{-1} m^{-3})	R^{300K}/R^{20K}
2259	5	10.74	529.5	0.474	4.98×10^{28}	0.793
A853	6.4	8.35	954	0.339	3.02×10^{28}	0.709
A854	7.5	10.84	387.9	0.453	4.74×10^{28}	0.809
A855	9.5	10.94	330.6	0.418	4.75×10^{28}	0.788
K1	3.154	12.7				0.83
K2	4.2	12.9	450	0.53	6.5×10^{28}	0.90
K3	5.81	14.6				
K4	7.47	14.8				1
K5	8.632	15.35				
K6	9.96	10.8	90			1.025
K7	14.94	16				
K8	21.58	16.35				1.023
K9	33.2	16.35				

III. EXPERIMENT AND RESULTS

A. DC transport and superconducting properties

Transport measurements were carried out by the standard four-probe technique in a Physical Property Measurement System (PPMS) manufactured by Quantum Design. Applied bias currents were less than 100 μA. The square resistance, R_S, was measured with the van der Pauw method that eliminates the effect of the planar geometry for 2-d specimens. In Fig. 1 we show $R_S(T)$ dependences for four NbN films with different thicknesses.

As it is seen in the inset, for each film R_S increases with the decrease in the temperature from 300 K down to approximately 20 K that is most likely due to weak-localization [44]. At lower temperatures the $R_S(T)$ dependences flatten, the square resistance of each film reaches a plateau and then goes down to zero value within a finite transition region caused by superconducting fluctuations.

Presence of two types of excitation: topological (magnetic vortices) and electronic (quasiparticles) complicates definition of the superconducting transition temperature in two dimensional (2-d) films. It turns out that highly resistive 2-d superconducting films exhibit two transition temperatures. One of them, T_{BKT} (Berezinskii-Kosterlitz-Thouless), controls unbinding of vortex-antivortex pairs that provides emergence and an exponential rise of the resistance with increasing density of free vortices. The other controls the energy gap. It is known as the mean-field transition temperature and doesn't cause the emergence of the resistance. In Ref. 28 it was reported that for NbN film with R_{SN} = 431 Ohm/sq these temperatures are related as $T_{BKT} = 0.85T_C$. Anyway, right above the superconducting transition, our experimental $R_S(T)$ dependences are well described by the theory of fluctuation conductivity of Aslamazov and Larkin (AL) [46] and Maki and Thompson (MT) [47, 48]. For two dimensional films the theory predicts

$$R_S(T) = \frac{R_{SN}}{1+R_{SN}\frac{1}{16}\frac{e^2}{\hbar}\left(\frac{T_C}{T-T_C}\right)}, \quad (1)$$

where $\hbar$ is the reduced Planck constant, e is the elementary charge, T_C is the BCS mean-field transition temperature and R_{SN} is the normal-state square resistance at temperature right above the superconducting transition. We used T_C and R_{SN} as fitting parameters to fit experimental data in the range $0.9R_{SN} \le R_{SN}(T) \le R_{SN}$ (solid lines in Fig. 1). Best fit parameters are listed in Table II. Appling external magnetic field perpendicularly to the film surface, we measured $R_S(T)$ dependences for a set of magnetic fields. The preset field was taken as the critical field at the temperature which corresponds to the midpoint of the transition, i.e. $R_S = R_{SN}/2$. This gives the second critical magnetic field, H_{C2}, as a function of temperature for the temperature range below T_C. For all our films, we found almost linear behavior of H_{C2} vs T in the range $T_C/2 < T < T_C$ and used the slope for computing the electron diffusion coefficient as [49]

$$D = \frac{4k_B}{\pi e}\left(\frac{dH_{C2}}{dT}\right)^{-1}. \quad (2)$$

The values of D are listed in Table II along with the total electron density of states at the Fermi energy, $N(0)$, which we computed using Einstein relation $N(0) = 1/(e^2 R_{SN} d D)$.

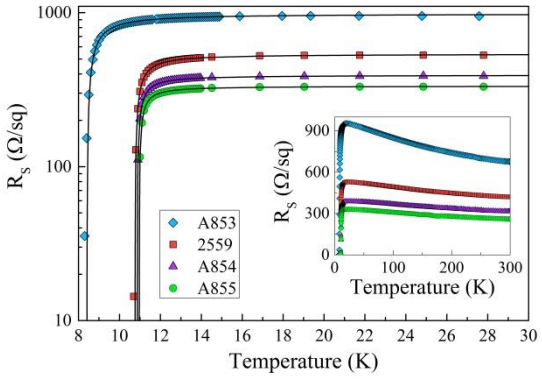

Fig.1. Temperature variation of the square resistance for four exemplarily films with different thicknesses around their superconducting transitions. Solid lines represent the best fits obtained with Eq. (1). The inset shows resistances in the larger range up to 300 K.

B. Magnetoconductance

Films (2259, A853, A854, A855) represent disordered 2-d systems suitable for MC method. We use the same PPMS apparatus as for DC measurements, to acquire square resistance $R_S(H,T)$ at different fixed temperatures in the range from T_C to $3T_C$ by varying magnetic field in the range from 0 to 9 T. The dimensionless change in the conductance per sample square induced by the field at the fixed temperature T was determined according to

$$\delta\sigma(H,T) = \frac{2\pi^2\hbar}{e^2}\left[\frac{1}{R_S(H,T)} - \frac{1}{R_S(0,T)}\right]. \quad (3)$$

Experimental data are shown in Fig. 2. Since dependences $\delta\sigma(H,T)$ are monotonous and look pretty similar for all studied specimens, we plot in Fig. 2 data for only one representative film.

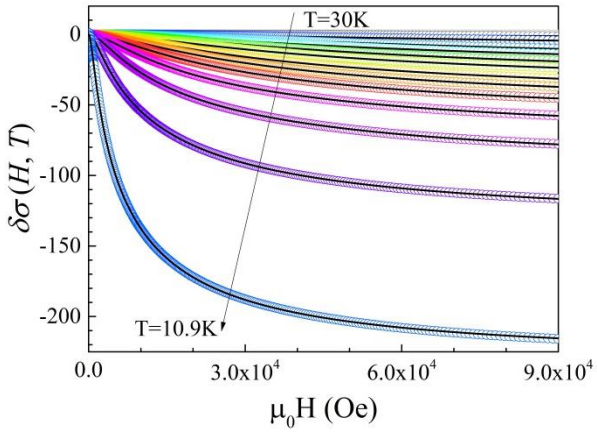

Fig.2. Field induced change in the magnetoconductance (Eq.(3)) for the film 2259 vs magnetic field. Different colors correspond to different temperatures. Solid black curves are fits with Eqs. (4) – (7).

Contribution to the magnetoconductance $\delta\sigma(H,T)$ due to the effect of weak localization has the form [50]

$$\delta\sigma^{WL}(H,T) = \frac{3}{2}\psi\left(\frac{1}{2}+\frac{H_2}{H}\right) - \frac{1}{2}\psi\left(\frac{1}{2}+\frac{H_i}{H}\right) + \frac{3}{2}\ln\left(\frac{H}{H_2}\right) - \frac{1}{2}\ln\left(\frac{H}{H_i}\right), \quad (4)$$

where $\psi(x)$ is the di-gamma function, $H_i = \hbar/(4eD\tau_\varphi)$ is called the inelastic magnetic fields, τ_φ is the phase breaking time, $H_2 = H_i + \frac{4}{3}H_{s.o.}$, $H_{s.o.} = \hbar/(4eD\tau_{s.o.})$, and $\tau_{s.o.}$ is the spin-orbit scattering rate. The WL correction provides positive contribution to $\delta\sigma(H,T)$; its magnitude decreases with the increase of magnetic field. At temperatures such that T - T_C > T_C, WL contribution to the magnetoconductance is much larger than corrections due to fluctuations.

Superconducting fluctuations (stochastic formation of Cooper pair) decrease the time that electrons remain normal, i.e. decrease their mean concentration and increase effective conductance. This causes broadening of the superconducting $R_S(T)$ transition at $T > T_C$. Since the increase in conductivity due to fluctuations is reduced by the external magnetic field, fluctuations provide negative contribution to $\delta\sigma(H,T)$. The effect is commonly denoted as Aslamazov-Larkin correction to magnetoconductance. In the 2-d limit and in the immediate vicinity of T_C, where the AL contribution dominates $\delta\sigma(H,T)$, it has the form [46, 51]

$$\delta\sigma^{AL}(H,T) = -\frac{\pi^2}{8\ln\left(\frac{T}{T_C}\right)}\left[8\left(\frac{\tilde{H}_C}{H}\right)^2\left\{\psi\left(\frac{1}{2}+\frac{\tilde{H}_C}{H}\right) - \psi\left(1+\frac{\tilde{H}_C}{H}\right) + \frac{H}{2\tilde{H}_C}\right\} - 1\right]. \quad (5)$$

Here $\widetilde{H}_{\mathrm{C}}$ is the characteristic field defined by the relation $\widetilde{H}_{\mathrm{C}} = C\,\frac{k_B T}{\pi e D}\ln\left(\frac{T}{T_{\mathrm{C}}}\right)$. In different publications the numerical factor *C* were assigned values from 2 to 6 [44, 52-55].

Maki-Thompson correction to magnetoconductance accounts for stochastic, for a time shorter than τ_φ, pairing of two electrons, which are about to simultaneously (coherently) scatter at the same impurity. Paring eliminates scattering that effectively increases the electron mean free path and weakens the effect of localization. Since in the 2-d limit localization causes correction to conductance $\delta\sigma \propto -\ln(L_\varphi/l)$ (L_φ is the phase breaking length), such events give positive contribution to $\delta\sigma(H,T)$. MT correction [47, 48] for the 2-d limit was elaborated by Larkin [56]. The contribution is given by

$$\delta\sigma_{(*)}^{\mathrm{MT}}(H,T) = -\beta_{\mathrm{L}}(T)\left[\psi\left(\tfrac{1}{2}+\tfrac{H_{\mathrm{i}}}{H}\right)+\ln\left(\tfrac{H}{H_{\mathrm{i}}}\right)\right], \tag{6}$$

where $\beta_{\mathrm{L}}(T) = \pi^2/[4\ln(T/T_{\mathrm{C}})]$ at $\ln(T/T_{\mathrm{C}}) \ll 1$. The MT contribution was further modified by Lopes dos Santos and Abrahams (LSA) for the temperatures close to T_{C} ($\ln(T/T_{\mathrm{C}}) \ll 1$) [57] as

$$\delta\sigma_{(\mathrm{mod})}^{\mathrm{MT}}(H,T) = -\beta_{\mathrm{LSA}}(T,\delta)\left[\psi\left(\tfrac{1}{2}+\tfrac{H_{\mathrm{i}}}{H}\right)-\psi\left(\tfrac{1}{2}+\tfrac{\widetilde{H_{\mathrm{C}}}}{H}\right)-\ln\left(\tfrac{\widetilde{H_{\mathrm{C}}}}{H_{\mathrm{i}}}\right)\right], \tag{7}$$

where $\beta_{\mathrm{LSA}}(T,\delta) = \pi^2/\{4\,[\ln(T/T_{\mathrm{C}})-\delta]\}$ and $\delta = \pi e D H_{\mathrm{i}}/(2k_{\mathrm{B}}T)$ is the MT pair-breaking parameter [58-60].

We fit experimental data in Fig.2 combining WL contribution with fluctuation corrections discussed above. For temperatures well above T_{C} the sum of Larkin's expression for the MT correction (Eq.(6)) and the WL contribution (Eq. (4)) was used; for temperatures still above but much closer to T_{C} we used the sum LSA correction (Eq.(7)) and the WL contribution (Eq.(4)); for temperatures at the immediate vicinity of T_{C} we added AL correction (Eq.(5)) to this sum. Although borders between these temperature intervals are rather intuitive, they are easy to define. For example, including the AL term at intermediate temperatures makes it impossible to fit the experimental data at all. In the fitting procedure we used H_{i}, $H_{\mathrm{s.o.}}$, and β_{LSA} as fitting parameters. Associating τ_φ with the inelastic scattering time, we found its best fit value as $\tau_{\mathrm{in}} = \hbar/(4eDH_{\mathrm{i}})$. In Fig. 3a we show $1/\tau_{\mathrm{in}}$ as a function of temperature.

The total inelastic scattering rate extracted from magnetoconductance measurements is the sum of rates affiliated with independent inelastic interactions in which electrons are involved. They are electron-electron interaction (*e-e*) [661], electron-phonon interaction (*e-ph*) and electron-fluctuation interaction (*e-fl*). The latter is associated with the loss of the electron energy and phase coherence due to recombination of electrons into superconducting pairs [62]. Hence, the total inelastic scattering rate is given by $\tau_{\mathrm{in}}{}^{-1} = \tau_{\mathrm{in(e-e)}}^{-1} + \tau_{\mathrm{in(e-ph)}}^{-1} + \tau_{\mathrm{in(e-fl)}}^{-1}$. The contributing rates are:

$$\begin{cases} \tau_{\mathrm{in(e-e)}}^{-1} = \frac{k_B T}{\hbar}\frac{1}{2C_1}\ln(C_1) \\ \tau_{\mathrm{in(e-ph)}}^{-1} = C_2 T^{\mathrm{n}} \\ \tau_{\mathrm{in(e-fl)}}^{-1} = \frac{k_{\mathrm{B}} T}{\hbar}\frac{1}{2C_1}\frac{2\ln(2)}{\ln(T/T_{\mathrm{C}})+B} \end{cases} \tag{8}$$

where $C_1 = \pi\hbar/R_{\mathrm{SN}}e^2$, $B = 4\ln(2)/\left[\sqrt{\ln(C_1)^2 + 128C_1/\pi} - \ln(C_1)\right]$ [62]. At the second stage we use C_1 and *n* as fitting parameters to fit the temperature dependence of the experimental scattering rate $\tau_{\mathrm{in}}{}^{-1}(T)$ with the sum of contributions (Eq. 8) due do different scattering processes. The result is shown in Fig. 3a for four different films. Inset in Fig. 3a shows the total rate $1/\tau_{\mathrm{in}}(T)$ for the film A855 (thick green curve) and all three contributions separately (black thin curves). It is clearly seen that at $T >> T_{\mathrm{C}}$ the term $\tau_{\mathrm{in(e-ph)}}^{-1}$ dominates and defines both the temperature dependence and the magnitude of the inelastic scattering rate. Contrarily, close to T_{C} the term $\tau_{\mathrm{in(e-fl)}}^{-1}$ dominates and controls the upturn in the $\tau_{\mathrm{in}}{}^{-1}(T)$ dependence.

Since the scope of the present study is limited to processes affecting relaxation of the excess electron energy, we restrict ourselves to temperatures above 14 K where *e-ph* scattering rate dominate. Fig. 3b shows experimental data for $\tau_{\mathrm{in}}{}^{-1}$ in the temperature range from 14 to 30 K and the best fits obtained with the second term in Eq. (8). The best fit values of the exponent, *n*, in $\tau_{\mathrm{in(e-ph)}}^{-1} \sim T^n$ dependences along with the extrapolated values of $\tau_{\mathrm{in(e-ph)}}$ and $\tau_{\mathrm{in(e-e)}}$ at 10 K are listed in Table III.

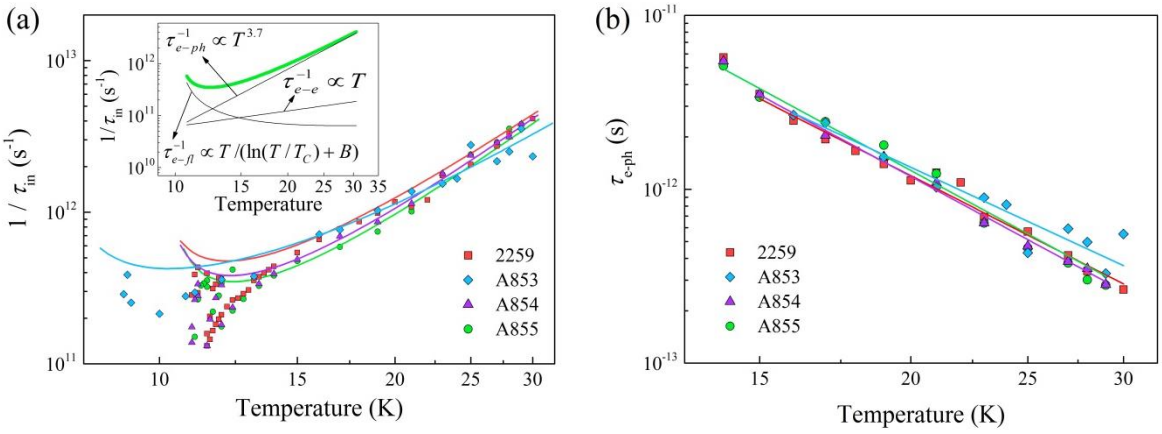

Fig.3. (Color online) (a) Inelastic scattering rate vs temperature (symbols) extracted from magnetoconductance measurements in the double logarithmic scale. Solid lines are fits made with the sum of all three terms in Eq. (8). The inset shows the best fitting curve for the film A855 film (thick line) and separately all three terms (thin lines). (b) *e-ph* interaction time vs temperature extracted from magnetoconductance measurements in the double logarithmic scale. Symbols correspond to experimental data; solid lines are fits according to the second term in Eq. (8) (the fitting parameters are listed in Table III).

Table III. Parameters of NbN on Si/SiO_2 substrate. Heat capacity ratios refer to the transition temperatures.

		Transport measurements (Sec. III A)			MC technique (Sec. III B)			TD technique (Sec. III C)	
sample	*d* (nm)	T_C (K)	D (10^{-4} m^2/s)	$N(0)$ (eV^{-1} m^{-3})	$\tau_{e\text{-}e}$ (10 K) (ps)	$\tau_{e\text{-}ph}$ (10K) (ps)	n $\tau_{e\text{-}ph} \sim T^{-n}$	τ_{esc} (ps)	c_e / c_{ph}
2259	5	10.74	0.474	4.98×10^{28}	10.8	11.9	3.53	33.5	0.5
A853	6.4	8.35	0.339	3.02×10^{28}	9.4	12.4	3.21	37.8	0.42 (0.26[a])
A854	7.5	10.84	0.453	4.74×10^{28}	13.4	15.9	3.75	45	0.48
A855	9.5	10.94	0.418	4.75×10^{28}	16.3	17.5	3.77	49.4	0.37

[a] The heat capacity ratio in brackets in the last column corresponds to the temperature 10.7 K.

Data in Table III show that for our films, the magnitude of $\tau_{e\text{-}ph}$ and its temperature dependence, extracted with the MC technique, don't obey any systematic dependence on the degree of disorder. Similar result was reported in Refs. [9] and [10]. Below (Section IV A) we apply the model of electron-phonon interaction in disordered metal films [8] to characterize the degree of disorder of our films in terms of the product $q_T l$. This allows one to estimate mass density of our films, phonon velocities and heat capacities for different phonon modes. We further use these parameters, along with the phonon velocities in substrates, to compute transmission coefficients and escape time

for phonons at studied film-substrate interfaces (Section IV B). These escape times are used in the next two sections as seed values for modeling the photoresponse of our films in the frameworks of the 2-T model.

C. Time-domain technique.

We studied photoresponse of superconducting microbridges to sub-picosecond pulses at the wavelength 800 nm with a repetition rate of 80 MHz. Microbridges with different thickness dependent length-to-width ratios were made from first four films listed in Table II. The values of the ratio were chosen to have for each microbridge the number of squares along the current path of the order of Z_0/R_{SN} where Z_0 = 50 Ohm is the impedance of the microwave pulse readout. Microbridges were mounted in a continuous flow cryostat with optical access through a quartz window. They were kept in the resistive state at an ambient temperature $T \geq T_C$ and biased by small dc current. The photoresponse of the bridge represents in the form of a voltage transient was amplified within a limited frequency band 0.1 - 5 GHz and recorded with a sampling scope. Fig. 4 shows voltage transients stored in the oscilloscope. Transients delivered by microbridges with different thicknesses look similar. They all, exhibit identical rising times. Obviously this time is limited to the bandwidth of the readout while the falling parts of the transients still contain valuable information. It is seen already in Fig. 4a that the impedance matching between the microbridge and the readout is not perfect that causes multiple reflections (signal ringing). In Fig. 4b, we plot the transients in the logarithmic scale that emphasizes the ringing and allows one to find out the ringing period of approximately 250 ps which corresponds to 2.5 cm electrical path between the microbridge and the first SMA connector at the microbridge holder.

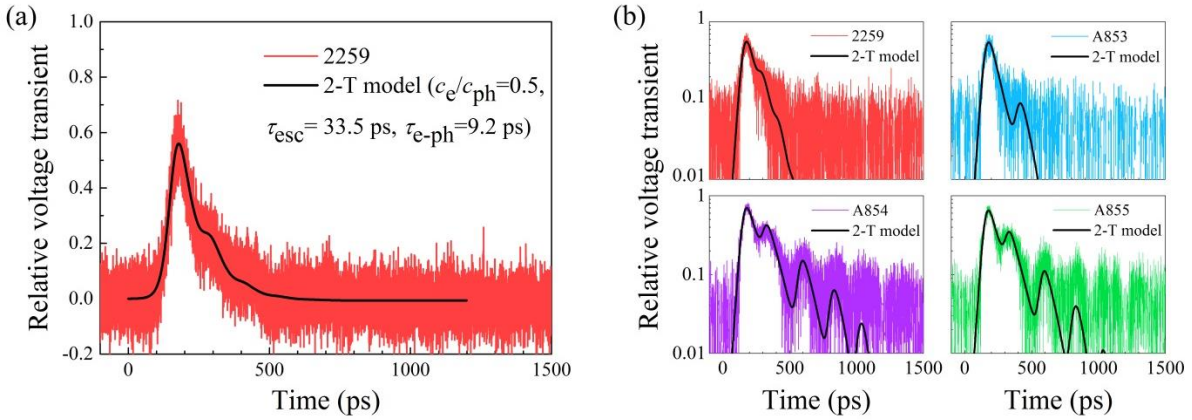

Fig. 4. (Colors online) (a) Voltage transient for the microbridge with the thickness 5 nm in the linear scale. (b) Voltage transients for NbN microbridges of four different thicknesses in the semi-logarithmic scale. Black curves are best fits according to Eqs. (9-13) with parameters: for 2259 c_e/c_{ph} = 0.5, τ_{esc} = 33.5 ps; for A853 c_e/c_{ph} = 0.42, τ_{esc} = 37.8 ps; for A854 c_e/c_{ph} = 0.48, τ_{esc} = 45 ps; and for A855 c_e/c_{ph} = 0.37, τ_{esc} = 49.4 ps, for each bridge τ_{e-ph} was fixed at the value obtained for original film from MC measurements. Legends specify film numbers from Table II.

In order to extract intrinsic interaction times we apply equations of the two-temperature model with pulse excitation [21]. This approach is commonly used to describe the non-equilibrium state created by optical pulse in a resistive or superconducting film [23]. With dimensionless units for time and energy, equations of the 2-T model look as follows:

$$\begin{cases} \frac{dT_e(\xi)}{d\xi} = -\Gamma_1(T_e(\xi) - T_{ph}(\xi)) + \frac{1}{d\,c_e} P_{RF}(\xi) + \frac{1}{c_e} P_{DC} \\ \frac{dT_{ph}(\xi)}{d\xi} = \Gamma_2(T_e(\xi) - T_{ph}(\xi)) - \Gamma_3(T_{ph}(\xi) - T_0) \end{cases}, \quad (9)$$

where T_e and T_{ph} - are temperatures of the electron and phonon subsystems, T_0 – is the bath temperature, $\Gamma_1 = \frac{\tau_0}{\tau_{e-ph}}$, $\Gamma_2 = \Gamma_1 \frac{c_e}{c_{ph}}$, $\Gamma_3 = \frac{\tau_0}{\tau_{esc}}$, $\xi = t/\tau_0$ is the dimensionless time $P_{RF}(t) = m^3 \xi^2 e^{-m\xi} E_0/\tau_0$ - analytical expression describing instantaneous power (the shape) of the excitation pulse. For m = 3.4, τ_0 represents the full width at half maximum and E_0 the total pulse energy absorbed by the unit area of the film. P_{DC} is the Joule power dissipated in the unit volume of the film. The magnitude of P_{DC} was extremely small in our measurements and therefore we neglected it. Solving Eqs. (9), we obtain time-dependent $T_e(\xi)$ and $T_{ph}(\xi)$ in the form.

$$\frac{T_e(\xi)-T_0}{T_0} = A_1 \frac{(\chi_1+\Gamma_2+\Gamma_3)}{\Gamma_2} e^{\chi_1 \xi} + A_2 \frac{(\chi_2+\Gamma_2+\Gamma_3)}{\Gamma_2} e^{\chi_2 \xi} + Q_1(\xi) e^{-m\xi},$$

$$\frac{T_{ph}(\xi)-T_0}{T_0} = A_1 e^{\chi_1 \xi} + A_2 e^{\chi_2 \xi} + Q_2(\xi) e^{-m\xi} \quad (10)$$

with parameters given by

$$\chi_{1,2} = -\frac{1}{2}\left(\sum_i^3 \Gamma_i \mp \sqrt{(\sum_i^3 \Gamma_i)^2 - 4\Gamma_1\Gamma_3}\right),$$

$$A_{1,2} = \pm \frac{\Gamma_2 E_0 m^3}{d\, c_e T_0} \frac{1}{(\chi_1-\chi_2)(m+\chi_{1,2})^3},$$

$$Q_2 = \frac{\Gamma_2\, E_0 m^3}{d\, c_e T_0}(a\,\xi^2 + b\,\xi + c), \quad (11)$$

$$Q_1 = \frac{E_0 m^3}{d\, c_e T_0}\big((\Gamma_2 + \Gamma_3 - m)(a\,\xi^2 + b\,\xi + c) + 2\,a\,\xi + b\big),$$

$$a = \frac{1}{2\,\gamma_1\,\gamma_2};\ \ b = \frac{(\gamma_1+\gamma_2)}{(\gamma_1\,\gamma_2)^2};\ \ c = \frac{(\gamma_1{}^2+\gamma_1\,\gamma_2+\gamma_2{}^2)}{(\gamma_1\,\gamma_2)^3};\ \ \gamma_{1,2} = m + \chi_{1,2}\,.$$

The photoresponse $V_{in}(\xi)$ is proportional to $T_e(\xi) - T_0$ (Eq. 10), to the steepness of the superconducting transition at the operation point and to the bias current. This initial transient is modified by the read out electronics (cables, bias-T, amplifiers, and sampling oscilloscope) with the finite bandpass. Transient characteristic of the read out, which is the output voltage transient in response to the unit vertical voltage step at the input, can be sufficiently good described as

$$h(\xi) = \left(1 - e^{-2\sqrt{2} f_C \xi}\right) \cdot e^{-2\sqrt{2} f_S \xi}, \quad (12)$$

where f_S and f_C – are the lower and the upper frequencies of the bandpass. Knowing $V_{in}(\xi)$, one can compute voltage transient at the oscilloscope with the Duhamel integral as

$$V_{out}(\xi) = \int_0^\xi \dot{V}_{in}(\xi')\, h(\xi - \xi')\mathrm{d}\xi'. \quad (13)$$

We used the formalism described by Eqs. 9 -13 to fit voltage transients recorded by the oscilloscope. Ringing was simulated by adding a series of equidistant identically shaped pulses with decreasing magnitudes. The best fit curves are shown in Fig. 4 with solid lines. There are four independent fitting parameters: the heat capacity ratio c_e/c_{ph}, the *e-ph* interaction time τ_{e-ph}, the phonon escape time τ_{esc} and the normalized pulse energy P_0/c_e. The latter changes only the magnitude of the transient and does not affect its shape. For each bridge we fixed τ_{e-ph} at the value obtained for original film from magnetoconductance measurements (Table III). We also fixed phonon escape time for the thickest microbridge A855 to be τ_{esc}= 49.4 ps according to the acoustic mismatch model (for details see Sec. IV B). For thinner samples we do not expect τ_{esc} to depend linearly on the thickness and allowed it to take values < 50 ps. This leaves two fitting parameters τ_{esc} and c_e/c_{ph} which were independently varied to

obtain the best fit. The best fit values are listed in Table III. Heat capacity ratios c_e/c_{ph} scatter in the range 0.37 – 0.5. These values agree reasonably well with previously reported. The phonon escape time increases from 33.5 ps for the 5 nm thick film (#2259) to 49.4 ps for the 9 nm thick film (A855) that corresponds to the prediction of the acoustic mismatch model.

D. Frequency domain technique

Frequency-domain measurements were done for K-series of NbN microbridges on sapphire substrates (Table II samples K1-K9). Film thickness varied from 3.2 to 33.2 nm. Data obtained with the frequency domain technique were partly reported in Refs. 37 and 43. The technique in detail was described in Ref. 43. Shortly, beams of two cw near infrared lasers (wavelength 850 nm) with the controllable difference between radiation frequencies were overlapped on the microbridge. Amplitude of the periodic variations of the photoresponse at the beating frequency f (the difference between frequencies of two lasers) was monitored for different beating frequencies in the interval from 10 MHz to 10 GHz. Similar approach (AMAR) described in Ref. 32 differs only in radiation frequencies which were in the sub-THz frequency range. For both frequencies, power of the absorbed radiation, P_{RF}, alternates periodically and causes modulation of the electron temperature. This leads to periodic sinusoidal variations in the photoresponse which are amplified and controlled with a spectrum analyzer. The roll-off frequency f_0 in the dependence of the photoresponse magnitude on the beating frequency $U(f)$ is the frequency at which the photoresponse magnitude decreases to one half of its value at small frequencies. For each microbridge we measured the roll-off frequencies at $T \approx T_C$ and extracted the response time $\tau_\varepsilon = (2\pi f_0)^{-1}$ which is plotted as a function of the film thickness in Fig. 5. Generally, τ_ε decreases when d decreases. However, the rate of the decrease is noticeably less for microbridges with smaller thicknesses. Analysis of the dependence of the response time on the film thickness by means of the phonon ray tracing is presented below in Sec. IV B.

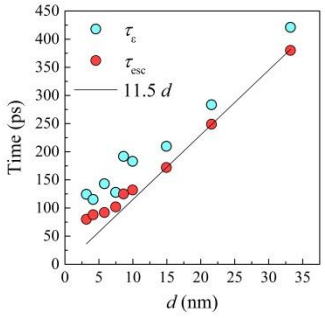

Fig. 5. Response time τ_ε vs thickness for NbN microbridges on sapphire substrates (open symbols). Best fit values of the phonon escape time vs thickness (red symbols). The best fit values of the ratio c_e/c_{ph} fall into the range 0.16 – 0.45. Black line represents the linear fit τ_{esc} = 11.5 d.

To obtain phonon escape times and heat capacity ratios in the framework of the FDAM technique we fit the entire $U(f)$ curve for each specimen with the 2-T model. We use Eq. (9) where we neglect dissipated Joule power and substitute pulse excitation with the periodic excitation in the form $P_{RF}(t) = P_0 e^{-j\omega t}$. Here $\omega = 2\pi f$ is the circular frequency and P_0 is the radiation power absorbed per unit area of the film. The solution for periodic excitation in the frequency domain was obtained by Perrin and Vanneste [16] and is given by

$$\frac{T_e(\omega)-T_0}{T_0} = P_0 \frac{1}{d\, C_e T_0} \frac{\tau_2\tau_3}{\tau_1} \frac{(1+j\omega\tau_1)}{(1+j\omega\tau_2)(1+j\omega\tau_3)}, \quad (14)$$

where characteristic times are $\tau_1 = (\Gamma_2 + \Gamma_3)^{-1}$ and $\tau_{2,3} = {\chi_{1,2}}^{-1}$, $\chi_{1,2}$ is defined in Eqs. 9 – 11 with $\Gamma_1 = {\tau_{\mathrm{e-ph}}}^{-1}$, $\Gamma_2 = \Gamma_1 \frac{c_\mathrm{e}}{c_\mathrm{ph}}$, $\Gamma_3 = {\tau_\mathrm{esc}}^{-1}$. The spectrum of the photoresponse (Eq. (14)) crucially depends on the heat capacity ratio $c_\mathrm{e}/c_\mathrm{ph}$. For instance, if $c_\mathrm{e} \gg c_\mathrm{ph}$ and $\tau_\mathrm{e-ph} \gg \tau_\mathrm{esc}$ Eq. 14 reduces to $T_\mathrm{e}(\omega) - T_0 \approx P_0\tau_2/(d\, c_\mathrm{e})(1 + j\omega\tau_2)^{-1}$, where $\tau_2 \approx \tau_\mathrm{e-ph} + \left(c_\mathrm{e}/c_\mathrm{ph}\right)\tau_\mathrm{esc}$. Exactly this limiting case is valid for thin Nb films [63]. It was also used for thin NbN films in several works [20, 22], however for NbN the required inequalities are not satisfied. Indeed, the ratio $c_\mathrm{e}/c_\mathrm{ph}$ estimated from our measurements (Sec. III C) as well as the ratios obtained in Ref. 33 (for 5.5 nm NbN film at T_C) and in Ref. 21 all give $c_\mathrm{e} < c_\mathrm{ph}$. This is why we used the full solution (Eq. 14) to fit our experimental data.

As it follows from MC measurements (Sec. III B, Table III) for films from the A series, $\tau_\mathrm{e-ph}$ as well as the exponent *n* don't differ much with the degree of disorder. Therefore, for les disordered films K1-K9 we expect close values of the factor *n* and close values of $\tau_\mathrm{e-ph}$ at 10K. Using the mean values (except the most disordered film A853) of the exponent *n* = 3.68 and the electron-phonon scattering time $\tau_\mathrm{e-ph}(10\ K)$ = 11.3 ps for films on silicon, we scaled this mean value to the actual transition temperatures of films on sapphire (K1 – K9, Table II) and obtained for them the expected interval of variation in $\tau_\mathrm{e-ph}(T_\mathrm{C})$ =8.3 – 3.2 ps. We used these values to fit experimental $U(f)$ curves with the 2-T model (Eq. 14). For thickest samples K7-K9, we additionally fixed τ_esc [ps] = 11.5 d [nm] according to the value computed in the framework of the acoustic mismatch model [5]. Computational details are presented in Sec. IV B. For thinner films K1-K6 we don't expect the phonon escape time to scale linearly with the thickness and allow τ_esc taking any value less than 150 ps. This approach leaves us two fitting parameters τ_esc and $c_\mathrm{e}/c_\mathrm{ph}$. In Fig. 5 we plot the best fit values of τ_esc as a function of film thickness. They vary from 75 ps for the thinnest film to 370 ps for the thickest film. For specimens thinner than 15 nm, τ_esc deviates from the linear dependence and tends to saturate. The best fit values of $c_\mathrm{e}/c_\mathrm{ph}$ monotonously vary from 0.16 for the film with *d* = 33.2 nm to 0.45 for the film with *d* = 3.2 nm.

It is worth mentioning here that the accuracy of extracting best fit values is different for FDAM and TDP techniques. For the range of fitting parameters typical for NbN, the same variation in the fitting parameters results in similar changes in fitting curves. However, in the TDP transients this change is more pronounced in the area with the lowest noise around the peak while in the FDAM spectra changes occur mostly beyond the cut-off in the area with largest noise.

IV. DATA ANALYSIS

Our results contain two important finding. First, the inelastic electron-phonon scattering rate depends on temperature as $1/\tau_\mathrm{e-ph} \propto T^\mathrm{n}$ with a weakly varying almost independent on the disorder and the film thickness factor $n \approx 3.2 \div 3.8$. Second, for the range of thicknesses less than 10 nm, the best fit value for the escape time obtained in the framework of the 2-T model does not linearly decrease any more with the film thickness. In the next subsection we show that the first finding complies with the Sergeev-Mitin model of electron-phonon interaction in dirty metal films [8]. The second finding reveals contribution of phonon trapping. We describe this effect below (section IV C) with the ray tracing approach to phonon propagation [14].

A. Electron-phonon scattering time

According to the SM model [8] the degree of disorder is controlled by the product $q_\mathrm{T}l$, where $q_\mathrm{T} = k_\mathrm{B}T/\hbar u$ is the wave vector of the thermal phonon and u is the sound velocity. In a strongly disordered metal $q_\mathrm{T}l >> 1$, the exponent, *n*, in the temperature dependence of the electron-phonon scattering rate $\tau_\mathrm{e-ph}^{-1} \propto T^\mathrm{n}$ can take a value between 2 and 4, depending on the degree of disorder and the property of impurities.

The inelastic scattering rate of an electron at the Fermi surface due to the interaction with longitudinal phonons (we use indices l and t to denote values associated with longitudinal and transverse phonon modes) is given by [8]

$$\tau_{\mathrm{e-ph(l)}}^{-1} = \frac{7\pi\varsigma(3)}{2\hbar}\frac{\beta_{\mathrm{l}}(k_{\mathrm{B}}T)^3}{(p_F u_{\mathrm{l}})^2} F_{\mathrm{l}}\left(q_{\mathrm{T(l)}}\, l\right). \tag{15}$$

In the expression above $\varsigma(n)$ is the Riemann zeta function and β is the dimensionless coupling constant. For both phonon modes it is given by $\beta_{\mathrm{l,t}} = (2E_{\mathrm{F}}/3)^2(N(0)/(2\rho u_{\mathrm{l,t}}^2))$. Here $E_{\mathrm{F}} = {p_{\mathrm{F}}}^2/(2m_{\mathrm{e}})$ is the Fermi energy, $p_{\mathrm{F}} = N(0)\pi^2\hbar^3/m_{\mathrm{e}}$ is the Fermi momentum, m_{e} is the electron mass, ρ is the mass density and $u_{\mathrm{l,t}}$ is the phonon velocity for particular mode. The effect of disorder on the scattering rate is controlled by the integral $F_{\mathrm{l}}(z) = \frac{2}{7\varsigma(3)}\int_0^{A_{\mathrm{l}}} dx\ \Phi_{\mathrm{l}}(xz)[N(x)+f(x)]x^2$, where *N(x)* and *f(x)* are Bose and Fermi distribution functions, and $\Phi_{\mathrm{l}}(x) = \frac{2}{\pi}\left(\frac{x\arctan(x)}{x-\arctan(x)} - \frac{3}{x}k\right)$ is the Pippard function. The upper limit of the integral $F_{\mathrm{l}}(z)$ is $A_{\mathrm{l,t}} = (6\pi^2)^{1/3}(l/a)/z$, where a is the size of the unit cell which is assumed for all films to be the same and equal to 0.44 nm. The parameter $1 \geq k \geq 0$ reveals the character of electron scatters; k = 1 corresponds to scatters vibrating in the same way as the host lattice, k = 0 corresponds to the static (i.e. 'non-vibrating') scatters such as heavy impurities and rigid boundaries. The inelastic electron scattering rate of an electron at the Fermi surface due to the interaction with transverse phonons is given by

$$\tau_{\mathrm{e-ph(t)}}^{-1} = 3\pi^2\frac{\beta_{\mathrm{t}}(k_{\mathrm{B}}T)^2}{(p_{\mathrm{F}}u_{\mathrm{t}})(p_{\mathrm{F}}l)} kF_{\mathrm{t}}\left(q_{\mathrm{T(t)}}\, l\right), \tag{16}$$

where $F_{\mathrm{t}}(z) = \frac{4}{\pi^2}\int_0^{A_{\mathrm{t}}} dx\ \Phi_{\mathrm{t}}(xz)[N(x)+f(x)]x$, and the Pippard function $\Phi_{\mathrm{t}}(x) = 1 + k\frac{3x-3(x^2+1)\arctan(x)}{2x^3}$. The apparent electron-phonon scattering rate is the sum of the two rates $\tau_{\mathrm{e-ph}}^{-1} = \tau_{\mathrm{e-ph(l)}}^{-1} + \tau_{\mathrm{e-ph(t)}}^{-1}$.

We fit our MC data (Sec. III B) using Eqns. 15-16. It turned out that the observed exponent in the temperature dependence of the scattering rate could be only reproduced with k = 1. In the temperature range where our MC data were acquired, the scattering rate of electrons via transverse phonons dominates and the parameter u_{l} does not affect the result of simulations. We therefore excluded u_{l} from the set of fit parameters and took it instantly twice as large as u_{t}. The relation $u_{\mathrm{l}} = 2u_{\mathrm{t}}$ is approximately valid for a large variety of materials. The remaining fit parameters are l, ρ and u_{t}. Their best fit values are listed in Table IV. We used the density of electron states computed from the data of transport measurements (Sec. III A) and the free electron mass (see Ref. [27] for verification) to obtain Fermi momentum and energy.

Table IV. Best fit values of the parameters in the SM model.

sample	l (nm)	ρ (g / cm^3)	u_{t} (m/s)
2259	0.13	7.8	2.42×10^3
A853	0.31	5.2	2.2×10^3
A854	0.14	7.5	2.4×10^3
A855	0.12	7.5	2.37×10^3

For all samples (except for the most disordered), the values of the electron mean free path l are by a factor of two smaller than the values obtained by different groups [25, 27, 29] from Hall-effect measurements, and by a factor of 4 to 6 smaller than the values reported in Ref. 24 where they were computed as $(3D\tau)^{1/2}$ from the measured diffusion constant and the elastic-scattering time. The latter was obtained by means of spectral ellipsometry. The best fit values of the velocity of transverse phonons and the mass density deviate from those reported in Ref. 64 where for bulk hexagonal NbN these parameters were found 4.5×10^3 m/s and 8.5 g/cm^3, respectively. Diversely, ρ and u_{t} obtained as fitting parameters for NbN are similar to those for TaN [65]. This finding correlates with remarkable similarity in superconducting properties of these two materials [67, 66]. A

smaller mass density correlates with the excess nitrogen content with respect to the optimal stoichiometry while reduced sound velocity is most probably the result of granularity.

B. Phonon escape time

We use the acoustic mismatch model by Kaplan [5] to compute phonon transmission coefficients for metal/substrate interfaces NbN/SiO_2 and NbN/Al_2O_3. The model describes acoustic plane waves associated with different phonon modes, which propagate through the interface between two isotropic semi-infinite media with zero attenuation, and takes into account mode conversion and total reflection at the interface. For instance, an incident longitudinal phonon (wave) is reflected and transmitted as pairs of longitudinal and transverse phonons (waves). Reflection and transmission coefficients depend on the angle of incidence, θ, propagation velocities of modes in both media and the deference between their acoustic impedances $Z_{1,2,\mathrm{i}} = u_{1,2,\mathrm{i}}\,\rho_{1,2}$ which are the products of the mass density of the medium and the propagation velocity of the particular mode in this medium. Indices 1 and 2 here refer to the film and the substrate, index i denotes the mode. Applying boundary conditions, which require continuity of the mechanical strain and stress at the interface, we found ratios of amplitudes of reflected and transmitted waves to the amplitude of the incident wave. Angle dependent transmission coefficients were defined separately for longitudinal, $\eta_{\theta\mathrm{l}}$, and two transverse, $\eta_{\theta\mathrm{ts}}$ and $\eta_{\theta\mathrm{tp}}$, modes as the ratio of the total energy flux of all transmitted modes to the energy flux of the incident mode $P_\mathrm{i} = \omega^2 Z_{1\mathrm{i}} A_\mathrm{i}^2 \cos\theta\,/2$ where A_i is the amplitude of the incident mode. Phonon escape time was defined for a flux of phonons propagating within a narrow solid angle at an incident angle θ and undergoing multiple sequential reflections at interfaces with the substrate and vacuum at the other side of the film. We define escape time for the mode as $\tau_{\mathrm{esc}}(\theta)_\mathrm{i} = P(t)(dP(t)/dt)^{-1}$ where $P(t)$ is the phonon flux remaining in the film. Right before the reflection with the number k the relative amount of $P(t)$ is $(1-\eta_{\theta\mathrm{i}})^{\mathrm{k}-1}$ and decreases after the reflection by the factor $1-\eta_{\theta\mathrm{i}}$. The time between two sequential reflections equals $2\,d/(u_\mathrm{i}\cos\theta)$ that results in the dimensionless rate of the decrease in the photon flux ${\tau_{\mathrm{esc}}(\theta)_\mathrm{i}}^{-1} = u_\mathrm{i}\eta_{\theta\mathrm{i}}\cos\theta\,/(2d)$. Integration over the solid angle gives the escape time per mode ${\tau_{\mathrm{esc\_i}}}^{-1} = u_\mathrm{i}\,\eta_\mathrm{i}/(4d)$ with $\eta_\mathrm{i} = \int_0^{\pi/2} 2\,\eta_{\theta\mathrm{i}}\sin\theta\cos\theta\,d\theta$. The total reflection of phonons at the interface is automatically accounted for by taking the real part of this expression. Since the decay rate of the photon energy through the particular mode is proportional to the heat capacity of the mode, which in turn is inversely proportional to the cube of the mode velocity, we found total weighted escape time ${\tau_{\mathrm{esc}}}^{-1} = \overline{\eta u}/(4d)$ where $\overline{\eta u} = \left[\eta_{\mathrm{ts}}u_\mathrm{t}^{-2} + \eta_{\mathrm{tp}}u_\mathrm{t}^{-2} + \eta_\mathrm{l}u_\mathrm{l}^{-2}\right] / \left[2u_\mathrm{t}^{-3} + u_\mathrm{l}^{-3}\right]$. Weighted values for the transmission coefficient and mode velocities were obtained in a similar way as $\bar{\eta} = \left[\eta_{\mathrm{ts}}u_\mathrm{t}^{-3} + \eta_{\mathrm{tp}}u_\mathrm{t}^{-3} + \eta_\mathrm{l}u_\mathrm{l}^{-3}\right] / \left[2u_\mathrm{t}^{-3} + u_\mathrm{l}^{-3}\right]$ and $\bar{u} = \left[u_\mathrm{t}^{-2} + u_\mathrm{t}^{-2} + u_\mathrm{l}^{-2}\right] / \left[2u_\mathrm{t}^{-3} + u_\mathrm{l}^{-3}\right]$. We have to note here that although $\overline{\eta u} \neq \bar{\eta}\,\bar{u}$ the difference between to sides of this inequality for studied interfaces remains less than ten per cent. Values of mass densities and sound velocities for substrates we took from Ref. 54. For NbN we used values obtained via fitting procedure in the framework of the SM model (Sec. IV A) and retained the assumption that the velocity of longitudinal phonons is twice as large as that of transverse phonons. We found for NbN/SiO_2 interface $\bar{\eta}$ = 0.28, $\bar{u}_1$= 2.54 × 10^3 m/s, $\bar{u}_2$= 4.35 × 10^3 m/s and for NbN/Al_2O_3 interface $\bar{\eta}$ = 0.12, $\bar{u}_2$= 6.87 × 10^3 m/s. For NbN/SiO_2 we obtained τ_{esc}[ps] =5.2 d [nm] and for NbN/Al_2O_3 τ_{esc}[ps] =11.54 d [nm], these values of phonon escape times are used in Sec. III C and D, respectively.

Computation that includes all three modes showed that through the NbN/Al_2O_3 interface the energy is dominantly transferred via transverse modes $\eta_\theta \approx \eta_{\theta\mathrm{ts}} + \eta_{\theta\mathrm{tp}}$ and that η_θ decreases very slowly with the angle until the angle of total internal reflection $\bar{\theta}_{\max} = arcsin(\bar{u}_1/\bar{u}_2)$. Hence for the phonon ray tracing (Section IV C) we used simplified expression $\bar{\eta} = \overline{\eta_\theta}(\sin\bar{\theta}_{\max})^2$.

C. Phonon ray tracing

The reduced ability of phonons in thin films to transfer the energy from electrons to the substrate as well as the reduced transfer rate was first considered by W. Eisenmenger et al. [14]. They described the effect of phonon trapping and the total reflection angle at the film-substrate boundary to the experimental recombination rate at low temperatures. The technique they used implies tracing of a phonon flux over several scattering events and boundary reflections to find its mean life-time in the film. The authors considered two different mean free paths of a phonon with the energy larger that the binding energy of a Cooper pair: Λ_w – the mean free path for reabsorption of the photon by a Cooper pair and Λ_v – the mean free path for inelastic phonon scattering on quasiparticle and bulk phonon losses. For temperatures close to the transition temperature, the binding energy of a Cooper pair (energy gap) is negligibly small that eliminates the difference between scattering rates of phonons on pairs and on quasiparticles. The intrinsic recombination time of quasiparticles becomes the electron-phonon interaction time τ_{e-ph} while the experimental recombination time appears as the decay time of the photoresponse τ_ε. Correspondingly, Λ_w is now the mean free path for the phonon-electron scattering and Λ_v represents the mean free path for bulk phonon losses.

With these redefinitions Eq. (51) from Ref. 14 takes the form

$$\frac{\tau_\varepsilon}{\tau_{e-ph}} = \left(1 + \frac{\Lambda_v}{\Lambda_w}\right) / \left(1 + \frac{1}{4}\frac{\Lambda_v}{\Lambda_w}\frac{\Lambda^*}{d}\, H_{av}\right), \tag{17}$$

where $1/\Lambda^* = 1/\Lambda_w + 1/\Lambda_v$, $H_{av} = (\sin\bar{\theta}_{max})^2\overline{\eta_\theta}\,(1-z)/(1-[1-\overline{\eta_\theta}]\,z)$ and $z = \exp(-2d/\Lambda^*)$.

We used Eq. (17) to analyze the decay time of the photoresponse, τ_ε, as a function of film thickness obtained with FDAM technique (Sec. III D, Fig. 6) for samples from the K-series. Since FDAM data points (Fig. 5) were obtained for each film at its own transition temperature, τ_{e-ph} varies from point to point. In order to fit experimental data in Fig 5 with Eq. 17, we used fixed τ_{e-ph} = 6.3 ps. This value relates to the film with a thickness of approximately 5 nm which corresponds to the intersection of the linear increase of τ_ε with d and the plateau defined by the thickness independent τ_ε at small d. Mean sound velocity for Al_2O_3 substrate, $\bar{u}_2$= 6.87 × 10^3 m/s, was calculated from the published data [5], and For NbN we used our best fit values (Table IV) to obtain $\bar{u}_1$= 2.54 × 10^3 m/s. Both result for NbN/Al_2O_3 interface in the angle of total internal reflection $\bar{\theta}_{max} = 21.8°$. The angle independent value $\overline{\eta_\theta}$ = 0.985 together with $\bar{\theta}_{max}$ above makes the product $(\sin\bar{\theta}_{max})^2\overline{\eta_\theta}\,\bar{u}_1$ equal to $\overline{\eta u}$ – the exact computed value of the integral over the entire solid angle (Section IV B). This approach leaves only two fitting parameters Λ_v/Λ_w and Λ_w. The best curve in Fig. 6 was obtained with the phonon mean free path Λ_w = 13 nm and $\Lambda_v/\Lambda_w = 615$ that evidences practical absence of bulk losses. The mean free path of phonons can be presented as $\Lambda_w = \tau_{ph-e}\,\bar{u}_1$ that directly gives the phonon-electron scattering time τ_{ph-e} = 5.1 ps. We relate this value to 13.5 K that is the expected transition temperature of a 5 nm thick film of the K-series. With the electron-phonon scattering and the detailed balance condition $\tau_{ph-e} = \tau_{e-ph}\,c_{ph}/c_e$, we found the heat capacity ratio c_e/c_{ph} = 1.6 which is by a factor of 4 larger than the ratio 0.45 obtained for these thinnest films from the best fits of the roll-offs with the 2-T model (Sec. III D). We note that in spite of fixed τ_{e-ph} value, Eq. (17) properly model the linear part of the $\tau_{esc}(d)$ dependence at relatively large thicknesses.

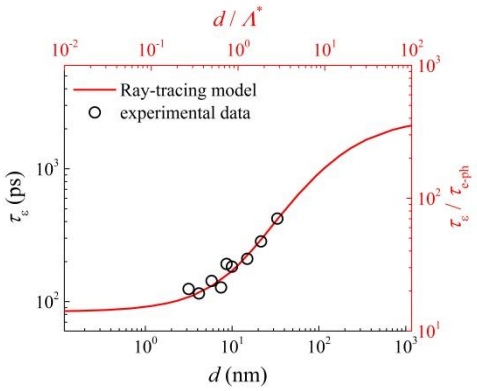

Fig. 6. Photoresponse time vs thickness for NbN microbridges on sapphire substrates (symbols, left and bottom axis). The data were obtained from frequency-domain measurements. Solid red line shows the best fit obtained with the phonon ray-tracing (top and right axis).

D. Discussion

When compared at the same temperatures, heat capacity ratios of thinnest films in K series is approximately 25% larger than capacity ratios obtained by means of TDP measurements for films from A series on silicon. This observation agrees with predictions of the Drude-Debye picture for electrons and phonons, $c_{\mathrm{e}} \propto N(0)\,T$ and $c_{\mathrm{ph}} \propto T^3$, if one takes into account the difference between densities of electron states (Table II) for these two film series.

Let us compare heat capacity ratio predicted by the Drude and Debye approaches with the ratios obtained experimentally as best fits in the framework of 2-T model and ray tracing. The Drude model predicts the electron heat capacity $c_{\mathrm{e}} = \frac{\pi^2 k_{\mathrm{B}}^2}{3} N(0)\,T$. For phonns, the 3-d Debye model predicts $c_{\mathrm{ph}} = \frac{2\pi^2 k_{\mathrm{B}}}{15}\left(\frac{k_{\mathrm{B}}\,T}{\hbar}\right)^3 \left[2\left(\frac{1}{u_{1\mathrm{t}}}\right)^3 + \left(\frac{1}{u_{1\mathrm{l}}}\right)^3\right]$. With $N(0)$ = 6.5×10^{28} eV^{-1} m^{-3} (Table II) and $u_{1\mathrm{t}} = u_{1\mathrm{l}}/2$ = 2.4×10^3 m sec^{-1} (Table IV) we obtained the heat capacity ratio $c_{\mathrm{e}}/c_{\mathrm{ph}}$ = 0.24 at T = 13 K (or $c_{\mathrm{e}}/c_{\mathrm{ph}}$ = 0.4 at T = 10 K). This value is slightly less than the values obtained via best fits of FDAM and TDP data in the framework of the 2-T model and makes only 20% of the value estimated from the detailed balance condition and the best fit value of the phonon-electron scattering time obtained via ray tracing. Why the Debye-Drude approach predicts smaller values of the heat capacity ratio is not clear. One of the possible explanations can be an absence of one of transverse phonon modes in thin films and reduced phonon density of states.

Since the ray tracing model and MC model do not require any knowledge on the heat capacities to obtain $\tau_{\mathrm{ph-e}}$ and, correspondingly, $\tau_{\mathrm{e-ph}}$ we consider this way of getting estimate for the heat capacity ratio more physically sound. The reason why the 2-T model provides smaller values of the ratio than the ray tracing is that 2-T model does not take into account phonon trapping, which is explicitly included in the ray tracing. Note that for the range of disorder and thicknesses specific for our films, the photoresponse time τ_ε (corresponds to the -3 dB roll-off in FDAM technique) computed in the framework of the 2-T model increases with the decrease of the phonon heat capacity (correspond to the increase in the $c_{\mathrm{e}}/c_{\mathrm{ph}}$ ratio). In fact only small fraction of phonons is emitted into the cone defined by the total internal reflection at the interface. These phonons quickly leave the film since for them interface transparency $\overline{\eta_\theta}$ = 0.985. The 2-T model offers to all phonons the very same transparency $\bar{\eta}$ = 0.124 which is a weighted average over all emission angles. This results in a larger value of τ_ε. To compensate for that in the framework of the 2-T model one needs to increase the best fit value of c_{ph}. Since in the fitting procedure with the 2-T model we found escape times close to the values computed by the acoustic mismatch model, the slow down

of the photoresponse due to phonon trapping is accounted for via phonon heat capacity. In this case the bottleneck parameter equal the ratio of best fit values of c_{ph} obtained by the 2-T model and by the phonon ray tracing. For our NbN films we thus found γ = 0.25 which is close to the phonon bottleneck parameter reported for thin WSi films [42].

We now estimate the Debye temperature of our films in the framework of the 3-dimensional Debye model as $T_D = \hbar(6\pi^2)^{1/3}\bar{u}_1/(k_{\mathrm{B}}a)$. Assuming a = 0.44 and $\bar{u}_1$= 2.54 × 10^3 m/s (Subsection IV B), we found T_D = 172 K. Such value is typical for Debye temperatures reported for similar films [27] and is a few times less than the values reported for bulk NbN. The reduction of the Debye temperature is due to phonon softening caused by granularity and weakening of ion bonds on film surfaces [41]. Even though the phonon softening is accounted for via mean sound velocity, the phonon heat capacity extracted from the fit with the ray tracing model is almost five times less than the value predicted by the three-dimensional Debye model. We attribute this difference to the reduction of phonon density of states and enhanced anisotropy of the phonon spectrum. Indeed, using the 3-D density of states from the Debye model and the average kinematic velocity for phonons $4u_{1\mathrm{t}}/3$ we arrive at q_T = 9 nm at 13 K. This value is twice as large as thicknesses of thinnest films in the K-series. The condition $q_T \geq d$ restricts available directions of the phonon wave vectors most efficiently within the cone with plane angle $\bar{\theta}_{\max}$ around the normal to the interface where $\eta_\theta > 1$ and where phonons can only escape from the film.

V. CONCLUSION

We have studied energy relaxation of electrons by means of magnetoconductance and photoresponse in a series of superconducting NbN films on Si/SiO_2 and Al_2O_3 substrates with thicknesses in the range from 3 to 33 nm. Our main results are:

(a) The inelastic electron-phonon scattering rate defined by MC technique depends on temperature as $1/\tau_{\mathrm{e-ph}} \propto T^{\mathrm{n}}$ with an exponent $n \approx 3.2 \div 3.8$. The magnitude of $\tau_{\mathrm{e-ph}}$ at 11 K falls into the range 11.9 - 17.5 ps. For our NbN films $\tau_{\mathrm{e-ph}}$ and the factor n show no systematic dependence on the degree of disorder.
(b) The Debye temperature in our films is noticeably smaller than one in the bulk NbN material. We attribute this to phonon softening caused by granularity and weakening of ion bonds at film surfaces.
(c) 2-T model allows describing photoresponse times in NbN films with the bottleneck parameter γ = 0.25 which is close to the value found for WSi films.
(d) The heat capacity of phonons obtained experimentally is smaller than the value expected for 3d Debye phonons with the estimated Debye temperature most likely due to reduced density of phonon states in thin films at low temperatures.

ACKNOWLEDGMENTS

M.S: acknowledges support by the Helmholtz Research School on Security Technologies, M.M. acknowledges support by the Russian Science Foundation (project No. 18-12-00364), the research has been carried out with the support of the Russian Science Foundation (project No. 17-72-30036). The authors would like to thank D. Henrich for sharing experimental results.

References

[1] D. Yu. Vodolazov, Single-Photon Detection by a Dirty Current-Carrying Superconducting Strip based on the Kinetic-Equation Approach, Phys. Rev. Appl. 7, 034014 (2017).

[2] Teun M. Klapwijk and A. V. Semenov, Engineering Physics of Superconducting Hot-Electron Bolometer Mixers, IEEE Transactions on Terahertz Science and Technology 7, pp. 627-648 (2017).

[3] A. Semenov and H.-W- Hübers, Bandwidth of a hot-electron bolometer mixer according to the hot-spot model, IEEE Transaction on Applied Superconductivity 11, pp. 196-199 (2001).

[4] A. A. Abrikosov, Fundamentals of the theory of metals, Elsevier Science Publishers B.V., Amsterdam, 1988

[5] Steven B. Kaplan, Acoustic matching of superconducting films to substrates, Journal of Low Temperature Physics Volume 37, Issue 3–4, pp 343–365, (1979).

[6] K. Smirnov, A. Divochiy, Y. Vakhtomin, P. Morozov, P. Zolotov, A. Antipov, V. Seleznev, NbN single-photon detectors with saturated dependence of quantum efficiency, Supercond. Sci. Technol. 31, 035011 (2018).

[7] D. Hazra, N. Tsavdaris, S. Jebari, A. Grimm, F. Blanchet, F. Mercier, E. Blanquet, C. Chapelier1 and M. Hofheinz, Superconducting properties of very high quality NbN thin films grown by high temperature chemical vapor deposition, Superconductor Science and Technology 29, No. 10, 105011 (2016).

[8] [7] A. Sergeev and V. Mitin, Electron-phonon interaction in disordered conductors: Static and vibrating scattering potentials, Phys. Rev. B 61, 6041 (2000).

[9] Liu J and Giordano N, "Electron-phonon scattering times in thin Sb films", Phys. Rev. B 43 3928 (1991).

[10] J. J. Lin, Tsang-Jou Li, and T. M. Wu, Electron-phonon scattering times in three-dimensional disordered Sb film, Phys. Rev. B 61, 3170 (2000).

[11] Bergmann G, Wei W, Zou Y and Mueller R M, Nonequilibrium in metallic microstructures in the presence of high current density, Phys. Rev. B 41 7386 (1990).

[12] A. I. Bezuglyj and V. A. Shklovskij, Kinetics of electron cooling in metal films at low temperatures and revision of the two temperature model, Journal of Physics: Condensed Matter, V. 30, N. 29 (2018).

[13] Mariia V. Sidorova,A. G. Kozorezov, A. V. Semenov, Yu. P. Korneeva, M. Yu. Mikhailov, A. Yu. Devizenko, A. A. Korneev, G. M. Chulkova, and G. N. Goltsman, Nonbolometric bottleneck in electron-phonon relaxation in ultrathin WSi films, Physical Review B 97, 184512 (2018).

[14] W. Eisenmenger, K. Laßmann, H. J. Trumpp, R. Krauß, Quasiparticle recombination and 2Δ-phonon-trapping in superconducting tunneling junctions, Appl. Phys. V. 11, 4, pp 307–320 (1976).

[15] A. Kardakova, A. Shishkin, A. Semenov, G. N. Goltsman, S. Ryabchun, T. M. Klapwijk, J. Bousquet, D. Eon, B. Sacépé, Th. Klein, and E. Bustarret, Relaxation of the resistive superconducting state in boron-doped diamond films, Phys. Rev. B 93, 064506 (2016).

[16] Perrin N. and Vanneste C., Response of superconducting films to a periodic optical irradiation, Phys. Rev. B. Vol. 28. P. 5150. 85 (1983).

[17] G N Gol'tsman, A D Semenov, Y P Gousev, M A Zorin, I G Godidze, E M Gershenzon, P T Lang, W J Knott and K F Renk, Sensitive picosecond NbN detector for radiation from millimetre wavelengths to visible light, Superconductor Science and Technology, V. 4, N. 9 (1991).

[18] K. V. Smirnov, A. V. Divochiy, Yu. B. Vakhtomin, M. V. Sidorova, U. V. Karpova, P. V. Morozov, V. A. Seleznev, A. N. Zotova, and D. Yu. Vodolazov, Rise time of voltage pulses in NbN superconducting single photon detectors, Appl. Phys. Lett. 109, 052601 (2016).

[19] Y. Pellan G. Dousselin J. PinelY. U. Sohn, Temperature and magnetic field dependence of NbN film resistivity: 3D weak localization effects, Journal of Low Temperature Physics, V. 78, 1–2, pp 63–77, (1990).

[20] S.Cherednichenko, P.Yagoubov, K.Il'in, G.Gol'tsman, and E.Gershenzon, Large bandwidth of NbN phonon-cooled hot-electron bolometer mixers on sapphire substrates, Eighth International Symposium on Space Terahertz Technology, Harvard University, (1997).

[21] A. D. Semenov, R. S. Nebosis, Yu. P. Gousev, M. A. Heusinger, and K. F. Renk, Analysis of the nonequilibrium photoresponse of superconducting films to pulsed radiation by use of a two-temperature model, Phys. Rev. B 52, 581 (1995).

[22] Yu. P. Gousev, G. N. Gol'tsman, A. D. Semenov, and E. M. Gershenzon, R. S. Nebosis, M. A. Heusinger, and K. F. Renk, Broadband ultrafast superconducting NbN detector for electromagnetic radiation Journal of Applied Physics 75, 3695 (1994).

[23] K. S. Il'in, M. Lindgren, M. Currie, A. D. Semenov, G. N. Gol'tsman, R. Sobolewski, S. I. Cherednichenko, and E. M. Gershenzon, Picosecond hot-electron energy relaxation in NbN superconducting photodetectors, Applied Physics Letters, vol. 76, no. 19, pp. 2752–2754, (2000).

[24] A. Semenov, B. Günther, U. Böttger, H.-W. Hübers, H. Bartolf, A. Engel, A. Schilling, K. Ilin, M. Siegel, R. Schneider, D. Gerthsen, and N. A. Gippius, Optical and transport properties of ultrathin NbN films and nanostructures, Phys. Rev. B 80, 054510 (2009).

[25] Destraz, Ilin, Siegel, Schilling, and Chang, Superconducting fluctuations in a thin NbN film probed by the Hall effect, Physical Review B 95, 224501 (2017).

[26] Y. Noat, V. Cherkez, C. Brun, T. Cren, C. Carbillet, F. Debontridder, K. Ilin, M. Siegel, A. Semenov, H.-W. Hübers, and D. Roditchev, Unconventional superconductivity in ultrathin superconducting NbN films studied by scanning tunneling spectroscopy, Phys. Rev. B 88, 014503 (2013).

[27] S. P. Chockalingam, Madhavi Chand, John Jesudasan, Vikram Tripathi, and Pratap Raychaudhuri, Superconducting properties and Hall effect of epitaxial NbN thin films, Phys. Rev. B 77, 214503 (2008).

[28] H. Bartolf, A. Engel, A. Schilling, K. Il'in, M. Siegel, H.-W. Hübers, and A. Semenov, Current-assisted thermally activated flux liberation in ultrathin nanopatterned NbN superconducting meander structures, Phys. Rev. B 81, 024502 (2010).

[29] S Ezaki, K Makise, B Shinozaki, T Odo, T Asano, H Terai, T Yamashita, S Miki and Z Wang, Localization and interaction effects in ultrathin epitaxial NbN superconducting films, J. Phys.: Condens. Matter 24 475702 (2012).

[30] B. Shinozaki, S. Ezaki, T. Odou, K. Makise, T. Asano, Superconducting Fluctuations above Tc and pair breaking parameters of two dimensional Niobium Nitride Films, Poster session presented at 28th International Conference on Low Temperature Physics, Gothenburg, Sweden, 9-16 August (2017)

[31] B. Shinozaki, S. Ezaki, T. Odou, K. Makise, T. Asano, Superconducting Fluctuations above Tc and pair breaking parameters of two dimensional Niobium Nitride Films, Journal of Physics: Conf. Series 969 (2018).

[32] Lu Zhang, Lixing You, Xiaoyan Yang, Junjie Wu, Chaolin Lv, Qi Guo, Weijun Zhang, Hao Li, Wei Peng, Zhen Wang & Xiaoming Xie, Hotspot relaxation time of NbN superconducting nanowire single-photon detectors on various substrates, Scientific Reports V. 8, 1486 (2018).

[33] E.M. Baeva, M.V. Sidorova, A.A. Korneev, K.V. Smirnov, A.V. Divochy, P.V. Morozov, P.I. Zolotov, Yu.B. Vakhtomin, A.V. Semenov, T.M. Klapwijk, V.S. Khrapai, and G.N. Goltsman, Thermal Properties of NbN Single-Photon Detectors, Phys. Rev. Applied 10, 064063 (2018).

[34] Y Dubi, Y Meir, Y Avishai, Nature of the superconductor–insulator transition in disordered superconductors, Nature 449 (7164), 876 (2010).

[35] R. Chicault and J. C. Villegier, New phonon structures observed by tunneling in granular NbN films, PHYSICAL REVIEW B Vol. 36, No. 10, pp. 5215-5224 (1987).

[36] R. Cabanel, J. Chaussy, J. Mazuer, J.C. Villegier, From localization to superconductivity in granular niobium nitride thin films, Journal de Physique 49 (5), pp.795-802, (1988).

[37] D. Rall, P. Probst, M. Hofherr, S. Wünsch, K. Il'in, U. Lemmer and M. Siegel, Energy relaxation time in NbN and YBCO thin films under optical irradiation, Journal of Physics: Conference Series, V. 234, P. 4 (2010).

[38] Gerd Bergmann, Quantitative analysis of weak localization in thin Mg films by magnetoresistance measurements, Physical Review B, Vol. 25, No 4, pp. 2937-2939 (1982).

[39] C. Gadermaier, A. S. Alexandrov, V. V. Kabanov, P. Kusar, T. Mertelj, X. Yao, C. Manzoni, D. Brida, G. Cerullo, and D. Mihailovic, Electron-Phonon Coupling in High-Temperature Cuprate Superconductors Determined from Electron Relaxation Rates, Phys. Rev. Lett. 105, 257001 (2010).

[40] Allen Rothwarf and B. N. Taylor, Measurement of Recombination Lifetimes in Superconductors, Phys. Rev. Lett. 19, 27 (1967).

[41] X.Y. Lang and Q. Jiang, Finite size effect on critical transition temperature of superconductive nanosolids, Solid State Communications 134 (2005) 797–801

[42] Xiaofu Zhang, Adriana E. Lita, Mariia Sidorova, Varun B. Verma, Qiang Wang, Sae Woo Nam, Alexei Semenov, and Andreas Schilling, Superconducting fluctuations and characteristic time scales in amorphous WSi, PHYSICAL REVIEW B 97, 174502 (2018)

[43] Dagmar Henrich, Influence of Material and Geometry on the Performance of Superconducting Nanowire Single-Photon Detectors, PhD thesis, Karlsruhe Institute of Technology (2013).

[44] Bergmann G, Quantum corrections to the resistance in two-dimensional disordered superconductors above Tc: Al, Sn, and amorphous Bi0.9Tl0.1 films, Phys. Rev. B 29 6114, (1984).

[46] L. G. Aslamazov and A. I. Larkin, The influence of fluctuation pairing of electrons on the conductivity of normal metal, Phys. Lett. 26A, 238, (1968).

[47] K. Maki, Critical Fluctuation of the Order Parameter in a Superconductor. I, Prog. Theor. Phys. 40, 193, (1968).

[48] R. S. Thompson, Microwave, Flux Flow, and Fluctuation Resistance of Dirty Type-II Superconductors, Phys. Rev. B 1, 327, (1970).

[49] P. G. de Gennes, Superconductivity of Metals and Alloys Benjamin, New York, p. 270, (1966).

[50] S. Hikami, A. Larkin, and Y. Nagaoka, Spin-orbit interaction and magnetoresistance in the two dimensional random system, Prog. Theor. Phys. 63, 707 (1980).

[51] Aslamazov, A.I. Larkin, Effect of Fluctuations on the Properties of a Superconductor Above the Critical Temperature, Sov. Phys. Solid State, 10(4), 875-880 (1968).

[52] Redi M H, Two-dimensional fluctuation-induced conductivity above the critical temperature, Phys. Rev. B 16 2027, (1977).

[53] Abrahams E, Prange R E and Stephen M J, Effect of a magnetic field on fluctuations above Tc, Physica 55 230, (1971).

[54] Tinkham M, Introduction to Superconductivity (Malabar, FL: Krieger) p 14, (1980).

[55] Wiesmann H, Gurvitch M, Ghosh A K, Lutz H, Kammerer O F and Strongin M, Estimate of density-of-states changes with disorder in A−15 superconductors, Phys. Rev. B 17 122, (1978).

[56] Larkin A I, Reluctance of two-dimensional systems, JETP Lett. 31 219, (1980).

[57] Lopes dos Santos J M B and Abrahams E, Superconducting fluctuation conductivity in a magnetic field in two dimensions, Phys. Rev. B 31 172, (1985).

[58] Thompson R S, The influence of magnetic fields on the paraconductivity due to fluctuations in thin films, Physica 55, 296-302, (1971).

[59] Char K and Kapitulnik A, Fluctuation conductivity in inhomogeneous superconductors, Z. Phys. B 72 253, (1988).

[60] Ebisawa H, Maekawa S and Fukuyama H, Pair breaking parameter of two-dimensional dirty superconductors, Solid State Commun. 45 75, (1983).

[61] B. L. Al'tshuler, A. G. Aronov, and D. E. Khmelnitzkii, Effects of electron-electron collisions with small energy transfers on quantum localization, J. Phys. C 15, 7367 (1982).

[62] W. Brenig, M. C. Chang, E. Abrahams, and P. Wolfe, Inelastic scattering time above the superconductivity transition in two dimensions: Dependence on disorder and magnetic field, Phys. Rev.B 31, 7001 (1985).

[63] A. V. Sergeev and M. Yu. Reizer, Photoresponse mechanisms of thin superconducting films and superconducting detectors, International Journal of Modern Physics BVol. 10, No. 06, pp. 635-667 (1996).

[64] Y. Zou, X. Wang, T. Chen, X. Li, X. Qi, D. Welch, P. Zhu, B. Liu, T. Cui, and B. Li, Hexagonal-structured ε-NbN: Ultraincompressibility, high shear rigidity, and a possible hard superconducting material, Sci. Rep. 5, 10811 (2015).

[65] J. Chang, G.-P.Zhao, X.-L. Zhou, K. Liu, andL.-Yu Lu, Structure and mechanical properties of tantalum mononitride under high pressure: A first-principles study, J. Appl. Phys. 112, 083519 (2012).

[66] A. Engel, A. Aeschbacher, K. Inderbitzin, A. Schilling, K. Il'in, M. Hofherr, M. Siegel, A. Semenov, and H.-W. Hübers, Tantalum nitride superconducting single-photon detectors with low cut-off energy, Appl. Phys. Lett. 100, 062601 (2012).

[67] K. Ilin, D. Henrich, Y. Luck, Y. Liang, M. Siegel, and D. Yu. Vodolazov, Critical current of Nb, NbN, and TaN thin-film bridges with and without geometrical nonuniformities in a magnetic field, Phys. Rev. B 89, 184511 (2014).